Journal of Applied Physics

RESEARCH ARTICLE | JANUARY 16 2026

Mo/Au transition-edge sensors: Effect of sensor size and absorber stem position on parameters and noise

Lourdes Fàbrega ; Agustín Camón ; Carlos Pobes ; Pavel Strichovanec ; J. Bolea

J. Appl. Phys. 139, 034502 (2026)
https://doi.org/10.1063/5.0303520

Journal of Applied Physics ARTICLE pubs.aip.org/aip/jap

Mo/Au transition-edge sensors: Effect of sensor size and absorber stem position on parameters and noise

Cite as: J. Appl. Phys. **139**, 034502 (2026); doi: 10.1063/5.0303520
Submitted: 22 September 2025 · Accepted: 26 December 2025 ·
Published Online: 16 January 2026

Lourdes Fàbrega,[1,a)] Agustín Camón,[2] Carlos Pobes,[2] Pavel Strichovanec,[2] and J. Bolea[3]

AFFILIATIONS

[1]Institut de Ciència de Materials de Barcelona (ICMAB-CSIC), Campus de Bellaterra, E-08193 Bellaterra, Spain
[2]Instituto de Nanociencia y Materiales de Aragón (INMA), CSIC-Universidad de Zaragoza, E-50009 Zaragoza, Spain
[3]Centro Universitario de la Defensa, Zaragoza, Spain

[a)]**Author to whom correspondence should be addressed:** lourdes@icmab.es

ABSTRACT

The basic transition parameters and excess noise of Mo/Au-based transition-edge sensor (TES) x-ray detectors without banks and with Au absorber are analyzed as a function of TES dimensions and absorber stems position. We show the effect of the absorber stems and TES dimensions on these parameters. We observe that the logarithmic derivatives of R(T) are reduced and develop non-monotonous behavior vs bias as stems are placed on the Mo/Au sensor area, progressively disturbing the current flow inside the TES. TESs with outer tangent stems display higher excess noise but also higher figures of merit because of their higher α and β values. We find that both longer and narrower TESs have higher excess noise so that a trade-off is required for TES performance optimization. We discuss some hints for that. The possible origins of the experimental excess noise of these devices are also explored and discussed.

INTRODUCTION

Transition-edge sensors (TESs) constitute radiation and particle detectors that exploit the superconducting transition of a thin film. They rely on the extremely sharp dependence of resistance on temperature within this transition region. The thin film is biased at some specific point within the transition and thermally connected to a colder bath via a thermal link, typically a Si_3N_4 membrane. When heat is deposited—usually through the absorption of a particle or a photon in an absorber or antenna thermally coupled to the TES—the sensor's resistance rises sharply. Under voltage bias, the resulting negative electrothermal feedback[1] drives the TES back toward equilibrium, generating a current pulse that corresponds to the detected event.

TESs form the basis of ultra-sensitive bolometers or microcalorimeters that are widely used, or envisioned for use, in advanced instruments for astrophysics, cosmology, quantum information, materials science, and other fields; for a general overview, see Refs. 2–14 and reviews.[15–17] Each application demands specific performance parameters—such as spectral resolution, noise-equivalent power, time response, and quantum efficiency—and, thus, requires tailored device designs. Understanding the relationship between the TES design and performance is, therefore, essential. The size and geometry of the superconducting film determine the transition mechanism and, thus, the dependence of resistance on temperature and current, R(T,J). Additional key factors include the properties of the radiation absorber (type, material, heat capacity, etc.) and the thermal links between TES, the absorber, and the thermal bath.

The performance of TESs is primarily governed by the sensitivities of their superconducting transition to temperature and current, as well as by excess—unexplained—noise. The sensitivities are quantified by the logarithmic derivatives of the device resistance with respect to temperature and current, denoted as α and β, respectively. The M parameter characterizes the Johnson-like excess noise that cannot be explained by the standard TES operation framework.[1]

Over the past two decades, numerous theoretical and experimental studies have been conducted,[18–39,15,16] aimed at optimizing performance of TES-based detectors for specific applications.

Despite significant progress and the remarkable performances achieved, a comprehensive understanding of the interplay between α, β, and M remains elusive. Theoretical models linking excess noise to the width of the superconducting transition include internal thermal fluctuation noise, weak link effects, the two-fluid model, and flux flow mechanisms.[26,29–32]

Experimental works determining α, β, and M in Mo-based and Ti-based TESs have explored factors such as the influence of normal metal structures,[18,24,27,28] device aspect ratio,[22,24,25,36,37,38] and the position of the absorber stems.[34] However, drawing general conclusions is challenging due to variability across devices. For instance, many studies of Mo-based TESs correspond to designs with the so-called banks: normal metal stripes along the edges, deposited to avoid Mo superconducting shorts and improve transition shape,[18–25,31] while some[24,26,39] do not. On the other hand, Ti/Au-based TESs do not have banks. Variations in the bias circuit, materials, geometry (length and width), sheet resistance, and different thermal conductance all may impact the nature of the superconducting transition and the excess noise—particularly influencing weak-link behavior.

We are developing Mo/Au-based TESs without banks or additional normal metal structures for x-ray detection. In previous work, we analyzed the effect of the aspect ratio on the α and β parameters of bare sensors without absorbers.[40] Here, we report on the α, β, and M parameters of TESs with gold x-ray absorbers, examining how these parameters depend on the TES size and the position of the absorber stems.

Our results show that α and β decrease and exhibit non-monotonic behavior with respect to bias, when the absorber stems are placed partially or entirely on the main sensor area, progressively disturbing current flow within the TES. Devices with absorber stems positioned tangentially at the outer edge show higher excess noise but also improved figures of merit due to their elevated α and β values. We also observe that longer and narrower TESs tend to exhibit greater excess noise. While we evaluated several common hypotheses for the origin of this excess noise, our results are inconclusive; however, certain trends emerge that may help in future device optimization.

EXPERIMENTAL

Mo/Au TESs without banks and with Nb/Mo leads were fabricated according to the process described in Ref. 41. The Si_3N_4 membrane is 0.5 μm thick and has a size of $250 \times 250\,\mu m^2$. Square Au absorbers of the lateral size 240 and 2.5 μm thickness were electrodeposited, using a Ti/Au seed layer of thickness 5 /100 nm deposited by electron beam evaporation. All the absorbers have four external stems lying on the membrane close to its corners, plus one or two stems lying on the TES or tangent to it. All stems have a height of 2.5 μm.

TESs analyzed in this work correspond to a wafer with normal square resistance $R_{sq} = 29\,m\Omega$ and critical temperatures T_c close to 109 mK, with different positions of the absorber stems in contact with the sensor and different TES sizes w × L, where w and L are, respectively, the width and length; the aspect ratio is, therefore, AR = L/w. Their basic parameters and names used in this paper are summarized in Table I, while their designs are shown in Fig. 1. Stems in contact with the TES and partially or totally outside the main Mo/Au rectangle area defining the sensor are thermally linked to it through a Mo/Au basis (an extension of the main Mo/Au rectangle constituting the TES), as shown in the case of design (c) and in Fig. 1 in the supplementary material; they may have circular or square base, as listed in Table I. Stems lying on the center of the TES are square, as are those on the membrane. Two devices from another wafer, without absorber and slightly different T_c, were characterized for the sake of comparison; they are also included in Table I.

Dark characterization under DC bias was performed in a Blueflors dilution refrigerator, as described elsewhere.[41] It included I–V curves at different bath temperatures T_{bath}, and complex impedance Z(ω) and noise spectra as a function of bias and T_{bath}, with frequency ranging between 10 Hz and 100 kHz. The shunt resistance of the bias circuit is 2 mΩ; no Nyquist inductor is used, and the total residual circuit inductance is 56 nH. The entire holder is magnetically shielded using a superconducting aluminum enclosure and a CRYOPERM shield. If any residual field B_{res} remains, it is compensated along the perpendicular direction using a Helmholtz coil, thus ensuring that the TES operates in a near zero-field environment. To estimate and compensate B_{res}, we bias the TES within its transition region and sweep the applied magnetic field to maximize the TES current. B_{res} rarely exceeds 0.6 μT.

Fits of the I–V curves were used to extract the TES thermal parameters and estimate T_c at each bias point; typical error bars for G are below 10% and below 0.1% for the transition temperature. The critical temperatures shown in Table I were extracted from the fits to the I–V curves at 50% R_n. The normal state resistance of the devices was obtained from the value at 200 mK, close to twice T_c.

In order to extract α, β, the heat capacity, and the time constant at each bias, Z(ω) data were fitted using the one thermal block (TB) model. This approximation works quite well for most devices, with the notable exception of TES 50 × 128a (see Fig. 2 in the supplementary material). A detailed inspection of the Z(ω) fits reveals increasingly noticeable deviations from the 1 TB behavior gradually appearing for the longer devices with higher aspect ratios (20 × 60c, 20 × 60d, 40 × 100b), suggesting that this simple model may not be suitable for long, elongated TESs. An examination of the error bars of the parameters extracted for representative devices and fits (see Fig. 3 in the supplementary material) indicates that the overall results and behavior discussed in this paper are reliable. Previously, we had also verified[42] that extracted β values using 1 and 2 TB differ slightly (few %). α values depend on the 2 TB configuration and can change in some cases significantly, although the bias dependence is not strongly affected. In light of this, and given that the main trends of α, β, and M of TES 50 × 128a are consistent with the qualitative behavior observed in the rest of the data sets reported here, we have included the results of TES 50 × 128a in this paper. However, we emphasize that both the poor fits to 1 TB and its anomalous G value suggest that its results should be interpreted with caution.

Noise spectra were fitted using the theoretical noise expected[1] from the experimental parameters obtained from Z(ω) (α, β, time constant, and heat capacity) and adding a Johnson-like excess noise term, M. As reported by other groups,[43] an excess phonon noise component (M_{ph}) was also required to fit the low frequency part of

TABLE I. Devices characterized in this work: TES size, absorber stems (size, shape, and position), normal state resistance, critical temperature and heat capacity, and thermal conductance to bath at 65% R_n. Also included is the estimated minimum width w_{min} of each TES because of the constriction caused by the stems in contact with Mo/Au. All devices display G values nearly proportional to their perimeter, except 40 × 100b and 50 × 128a, with G values moderately lower and significantly lower than the expected ones, respectively. Inspection of these TESs did not reveal any fabrication defect or device anomaly. Possibly related to these somehow anomalous G values, these two devices also display C values further from the average ones for the rest of TESs with absorber.

Device name in graphs	Size (w × L), μm	Stems on membrane, size (μm)	Stems in contact with TES			Minimum TES width (constriction) w_{min} (μm)	R_n (mΩ)	T_c (mK)	C @65% R_n (fJ/K)	G @ 65% R_n (pW/K)
			Position	Basis	Width (μm)					
40 × 80a	40 × 80	15	Central (a)	Square	10	30−2ξ*	56	108	1600	250
40 × 80b	40 × 80	15	Outer, tangent to edge (b)	Square	10	40−2ξ*	58	109	1600	270
60 × 60a	60 × 60	15	Central (a)	Square	10	50−2ξ*	29	109	1700	250
60 × 60b	60 × 60	15	Outer, tangent to edge (b)	Square	10	60−2ξ*	31	110	1700	270
20 × 60c	20 × 60	10	Inner tangent to edge (c)	Circular	5	10−2ξ*	81	108	1600	180
20 × 60d	20 × 60	10	Centered on the edge (d)	Circular	5	15−2ξ*	82	108	1700	180
30 × 100a	30 × 100	15	Central (a)	Square	10	20−2ξ*	94	107	1400	270
50 × 128a	50 × 128	15	Central (a)	Square	10	40−2ξ*	71	108	1200	210
40 × 100b	40 × 100	10	Outer, tangent to edge (b)	Circular	5	40−2ξ*	76	110	2200	240
60 × 80b	60 × 80	10	Outer, tangent to edge (b)	Circular	5	60−2ξ*	40	111	1800	250
40 × 80n	40 × 80		No absorber			40 (no constriction)	60	103	13	120
60 × 60n	60 × 60		No absorber			60 (no constriction)	30	104	13	125

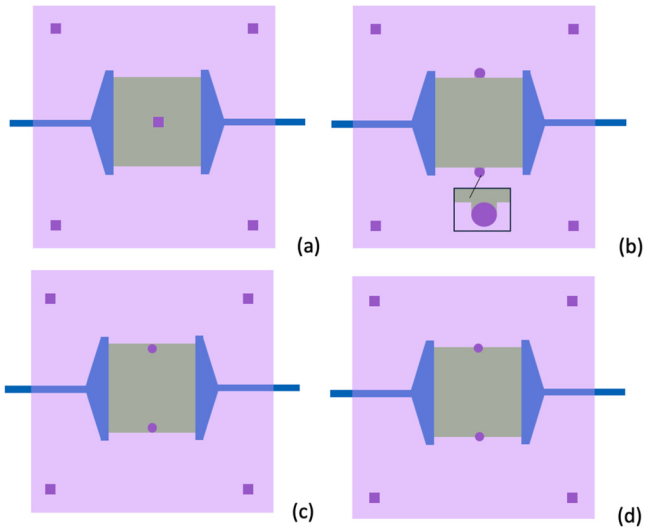

FIG. 1. Illustrations of the device layout showing the different positions of absorber stems in contact with the Mo/Au bilayer: (a) one central stem, (b) two outer stems tangent to the edges that delimit the w × L TES sensor rectangle area, (c) 2 inner stems tangent to the edges, and (d) two stems centered on the edges.

the spectra, see Fig. 4 in the supplementary material. Since phonon-like and Johnson-like noises dominate in different frequency ranges, no influence of M_{ph} on the extraction of M is expected. The uncertainty in the extracted M values is generally small (below 10%) but can become significant for very low data values, $M \leq 0.1$. Therefore, such small values are considered indistinguishable from $M = 0$. Missing data points in M graphs below (shown in the logarithmic scale) indicate that the Johnson-like excess noise M displays vanishingly small values ($M \leq 0.1$) for some devices/biases. This is the case, for instance, for TES 30 × 100a at all biases.

The spectral resolution was calculated from the noise spectra at each bias by using

$$\Delta E_{\mathrm{exp,noise}} = \frac{2\sqrt{2\ln(2)}}{\sqrt{\int_0^\infty \frac{4}{NEP(\omega)^2}\, d\omega}}. \quad (1)$$

The *NEP* here is the equivalent input-inferred power noise obtained using the measured current noise and current-to-power responsivity obtained from Z(ω) data fits to the 1 TB model.

Results reported here correspond to a bath temperature T_{bath} of 50 mK. Analysis of data at different T_{bath} between 50 and 80 mK has shown that the parameters in this study have a very small dependence on T_{bath}, for the explored temperature range. Data (not shown) of critical current as a function of the magnetic field, collected for the two devices without absorber, reveal traces of weak-link behavior for TES sizes 40 × 80 and 60 × 60, though considerably feeble; this is in agreement with earlier results on similar TESs.[40]

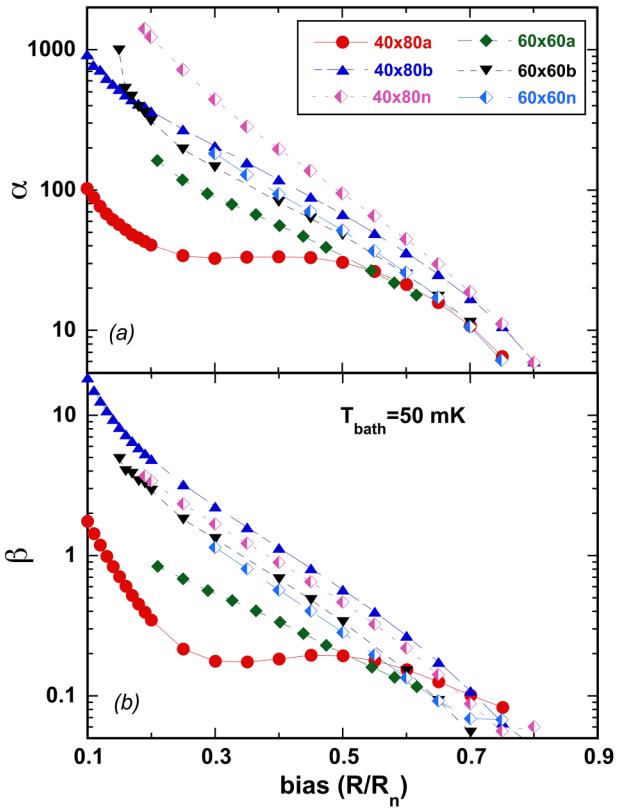

FIG. 2. Bias dependence of α (a) and β (b) at T_{bath} = 50 mK, for devices of sizes 40 × 80 and 60 × 60, without absorber and with absorber.

RESULTS

Figure 2 allows for a comparison of the effects of the presence of absorber stems on α and β, for TES dimensions 60 × 60 and 40 × 80. The bias dependences of both parameters in TESs without absorber are quite similar to those of TESs with absorbers displaying monotonous behavior in Fig. 3. They are also nearly identical both in value and bias dependence to those of similar TESs without absorber reported in a previous study,[40] highlighting the reproducibility of our devices. In particular, we note that both α and β are higher for the 40 × 80 TES than for the 60 × 60 one.

TESs without absorber exhibit higher α values than those with absorber; devices with outer tangent stems show α values that are closer to those of the absorber-free devices, indicating a progressive degradation of α as the stems increasingly influence current flow. In contrast, β is slightly lower in TESs without absorber than in the TES with this particular stem configuration.

A more detailed analysis of stem position is presented in Fig. 3, which shows α and β as a function of bias for all TESs with absorber listed in Table I. The values and bias dependences of both parameters are significantly affected by TES dimensions and absorber stem positions, especially at low and intermediate bias levels.

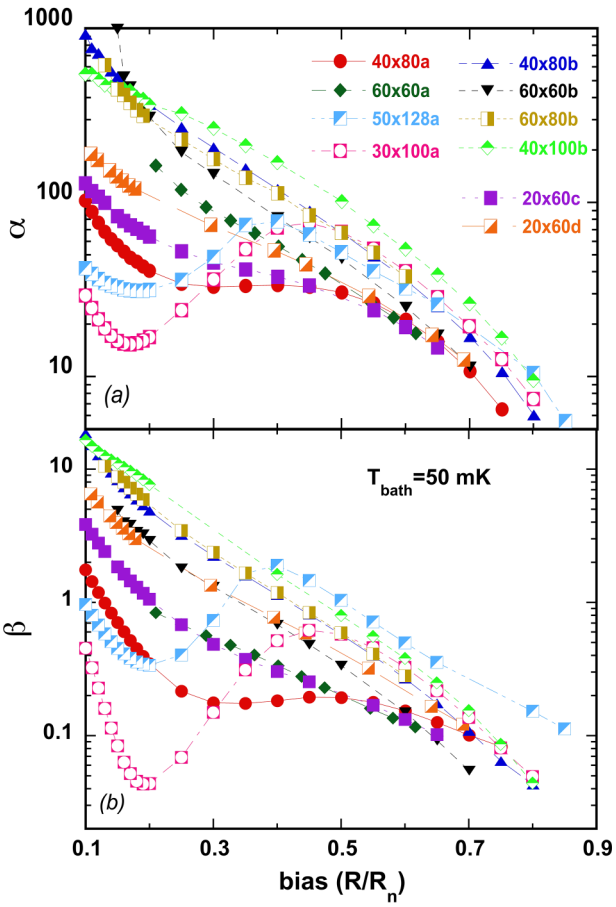

FIG. 3. Bias dependence of α (a) and β (b) at T_{bath} = 50 mK, for all the devices with absorber.

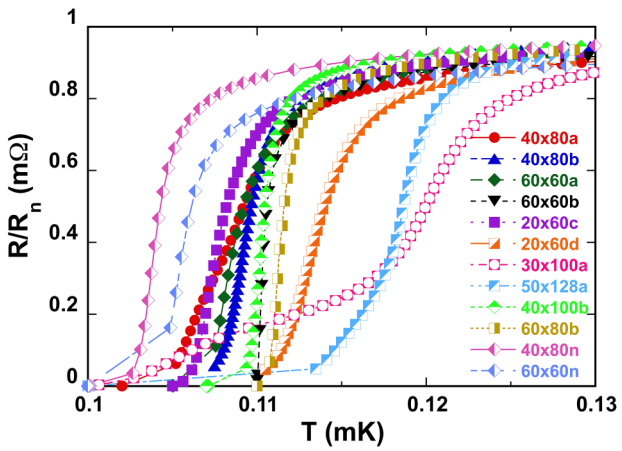

FIG. 4. R(T) transitions reconstructed from the I–V curves measured at the higher recorded T_{bath} which allows observation of superconducting behavior, for all TESs analyzed in the paper. TES 30 × 100a evidences a double transition, as expected from the behavior of α vs bias in Fig. 3(a). TES 50 × 128a, which also displays a minimum and a maximum in α and β vs bias, does not show an obvious double transition, though detailed inspection reveals an inflection, in correspondence with a sudden change of the derivative, i.e., α. Notice also the transitions of 20 × 60c, 20 × 60d, and 40 × 80a, somehow broader than the rest, in accordance with the slower decays observed in α vs bias.

α and β reach their highest values and show monotonous behavior in the four devices with outer tangent stems [design (b) in Fig. 1]. An inflection vs bias develops in devices with w = 20 μm and inner-tangent or on-the-edge stems [designs (c) and (d)] and is most pronounced in the TESs with a central stem [design (a)], which exhibit both a minimum and maximum, more noticeable in β. This trend (non-monotonous behavior) becomes more evident as the TES aspect ratio increases.

Interestingly, among the two TESs displaying intermediate behavior, that is, those with inner-tangent or edge-positioned stems—which are also those with the smallest width—the device with the stem fully inside the TES exhibits a more pronounced plateau, reinforcing the trend of the effect of inner stems, which in fact act as a constriction to current flow since the Mo/Au area under them is not superconducting. Also, because of the lateral inverse proximity effect, the region around the stems is expected to have superconductivity suppressed. Table I includes the minimum effective TES width w_{min} at the constriction caused by the stem, considering a lateral inverse proximity effect of extension of the order of the effective coherence length, ξ^*.[15] The superconducting current through the TES will circulate within w_{min}.

Among TESs with outer tangent stems—those exhibiting the highest α and β values—both α and β increase with length L. A comparison between the 60 × 80 and 40 × 80 devices suggests that the width w has minimal impact on α, at least within the size range studied. TESs without an absorber (Fig. 2) show similar trends with

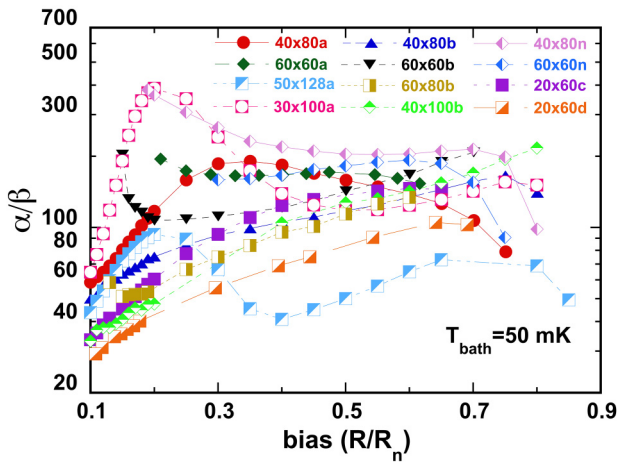

FIG. 5. Bias dependence of α/β at T_{bath} = 50 mK, for all the devices analyzed in this work.

respect to L and w. Even more, the two 20 × 60 TESs (one of them featuring inner-tangent stems, which, in principle, exert a similar constraint as a central stem) show higher and more monotonic α values than the 40 × 80a device (with central stem), thus corroborating the effect of increasing L—and, therefore, AR—on rising α and β. In opposition, among TESs with central stems lower α and β values are observed at low biases as the aspect ratio increases. Finally, at high bias levels and regardless of stem position, longer TESs yield higher α values, possibly due to the lack of rounding in the upper part of the R(T) transition, when the length of the TES is significantly larger than the effective superconducting coherence length, $L \gg \xi^*$.[44]

The non-monotonous behavior exhibited by α and β in some devices is indicative of the presence of a kink [a change in the derivative in the R(T) transition], which might in fact correspond to a change in the transition mechanism or a double superconducting transition. Inspection of the R(T) curves reconstructed from the I–V measurements (Fig. 4) indeed reveals a double transition in TES 30 × 100a, while 50 × 128a displays a broad transition with possibly a subtle kink. The origin of this behavior remains unclear. This could be related to the above discussed effects of the stems lying partially or totally on the TES rectangle area, inducing changes of the superconducting order parameter in the region around them because of the lateral inverse proximity effect. Nevertheless, three considerations must be noted. First, there is no correlation between the effective minimum width w_{min} and the significance of the non-monotonous behavior (either minima/maxima or kinks in α and β vs bias) observed for some devices. However, TESs exhibiting non-monotonous behavior share two features: (i) stems partially or entirely inside the rectangle defining TES area and (ii) widths equal or smaller than 40 μm. Second, observing a double transition requires a region along the TES length with a different T_c across the full cross-section. Since TESs 20 × 60c and 20 × 60d, with minimum constricted widths w_{min} of 10−2ξ^* and 15−2ξ^*, respectively, do not display clear double transitions, it is unlikely that TESs 30 × 100a and 50 × 128a, which have larger w_{min}, exhibit a double transition because of this reason. Third, a significant difference of TESs 30 × 100a and 50 × 128a compared to the others is their greater length. A possibility, to be investigated in future studies, could be that these TESs display significant variations of the superconducting critical temperature along their length due to the presence of the central stem and the longitudinal proximity effect.

Finally, the fact that TESs with the minimum constricted widths 10−2ξ^* and 15−ξ^* do not display double transitions also indicates an upper limit for the effective coherence length, $\xi^* < 5\,\mu$m. In Ref. 44, we showed that ξ^* is indeed expected to be of the order of ~μm.

The plot of α/β vs bias (Fig. 5) highlights that α is not proportional to β. Distinct behaviors are observed as a function of bias, indicating different R(T,I) dependences and, therefore, distinct superconducting regimes depending on the TES length and current distribution. In the low-bias region, most devices—except the two 60 × 60 TESs and those without absorber, which show a monotonously decreasing trend—display a steep rise in α/β with bias,

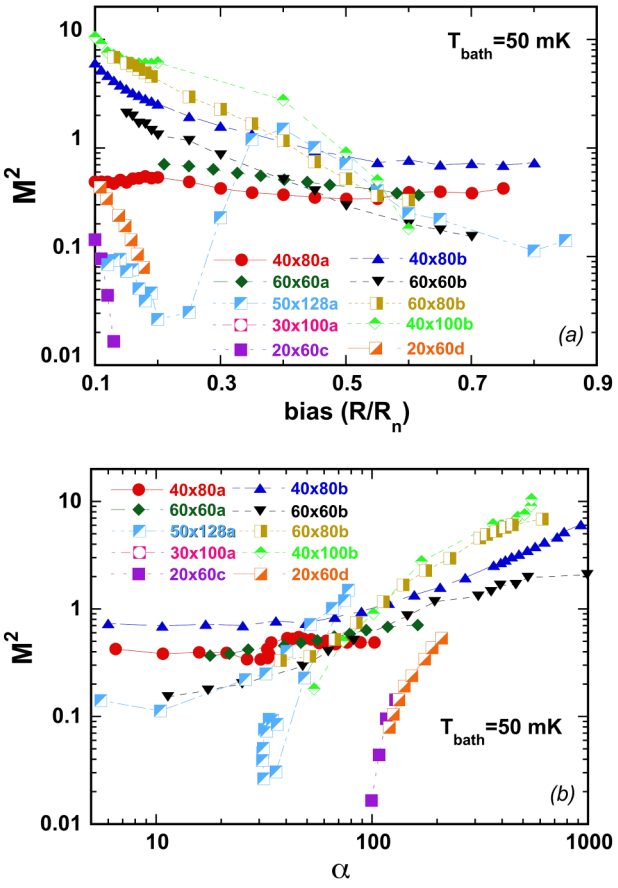

FIG. 6. (a) Dependence on bias of excess noise parameter M^2 at T_{bath} = 50 mK. (b) Dependence on alpha of excess noise parameter M^2 at T_{bath} = 50 mK.

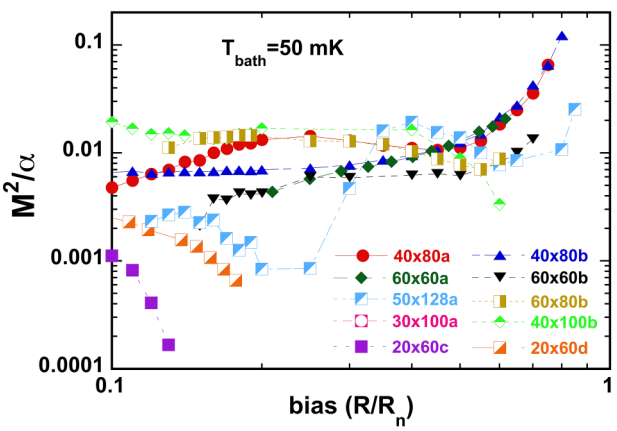

FIG. 7. M^2/α as a function of bias, T_{bath} = 50 mK.

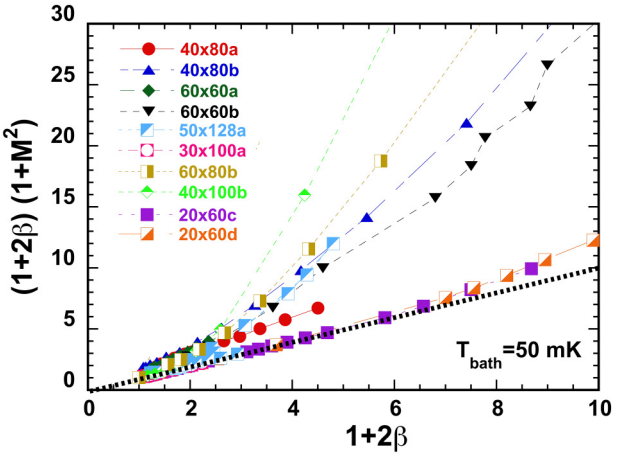

FIG. 8. Graph depicting the possible nonlinear effects on excess noise, for the lower M and β values; the data points indicate the tendency to increasing nonlinearities as M for higher M and β values. The line with slope 1 corresponds to $M = 0$.

which can be approximated by an exponential. At intermediate and high biases, and for TESs lacking local extrema in Figs. 3 or 5, the relationship between α and β can be roughly described by a power law, $\alpha \sim \beta^n$, as reported by other groups.[33,36,38,39,40] The exponent n ranges from 0.6 to 1, likely reflecting the approximated character of this functional dependence and the influence of the bias range selected for the fits.

Figure 6 shows M^2, the parameter quantifying Johnson-like excess noise, as a function of both bias and α. No clear correlation is found between M and TES perimeter, area, or thermal conductance to the bath. In general, M values are low, with only TESs with outer tangent stems exhibiting $M > 1$, particularly at low bias. Both longer L and narrower w tend to increase M. Among devices with the highest α and β (i.e., those with outer tangent stems), M correlates with the value of α: TES 40×100b shows the highest M, followed by 60×80b, 40×80b, and 60×60b. Although M generally increases with α, different functional dependences are observed. Particularly noteworthy are the two narrower TESs with on-the-edge or inner-tangent stems, which for $\alpha \sim 100$–200 and $\beta \sim 2$–10 (low biases) display lower M values than those corresponding to the other TESs in the same α and β value range. The low-bias branch of TES 50×128a follows a similar trend. This behavior deserves further analysis in the future, to clarify what originates it and, in particular, verify whether the low M values are due to some artifact.

Figures 7 and 8 further explore the relationships between M and α and β. Figure 7 shows M^2/α, which should remain constant if internal thermal fluctuation noise dominated the excess noise.[26] The graph reveals the variety of observed behaviors and values. M^2/α is only approximately constant for devices with outer tangent stems at low to intermediate biases. Significant dispersion in M^2/α at low bias is observed. Also, and again, the two narrower TESs with on-the-edge or inner-tangent stems (20×60c and 20×60d) and the lower bias part of 50×128a display a distinct behavior.

Figure 8 illustrates the nonlinear effects of β on noise. As expected, they are more prominent for higher β values. TESs with outer tangent stems and the higher bias branch of 50×128a display the greatest nonlinearities.

Attempts were made to test the dependences of M on β and bias using various noise models. Figure 9 plots the ratio $(1 + 2\beta)/(1 + M^2)/(1 + \beta)^2$, which should equal unity if two-fluid noise dominates M.[31] This is approximately the situation for several devices at intermediate and high biases. However, the model fails at low biases. Fits to the bias dependence expected for weak-link-dominated noise[30] were also attempted, but generally unsuccessful even at low biases. The lack of satisfactory fits to a single model suggests that multiple excess noise sources might be contributing, with varying weights depending on TES geometry and bias. In addition to the three possible origins of excess noise explored here, which are the most common reported so far, the motion of magnetic vortices might also be considered. Noise associated with magnetic flux flow was outlined in Ref. 32; however, the particular case of vortex depairing and subsequent motion at low biases, which was proposed in Ref. 45 as a possible mechanism for the appearance of finite resistance in TESs, would require further specific developments. Indeed, the conventional flux flow is an ohmic (i.e., linear) regime, in which the number of moving vortices, responsible for the resistance, is given by the external magnetic field. In the mechanism considered in Ref. 45, there is no external magnetic field, and the flux quanta able to move are unbound vortices and antivortices; this is a highly non-linear regime, in which current plays a relevant role. Therefore, the estimates in Ref. 32 may not hold and specific calculations are likely to be necessary.

Figure 10 shows the modified figure of merit including Johnson-like excess noise,

$$K' \equiv \frac{\alpha}{\sqrt{1+2\beta}} \frac{1}{\sqrt{1+M^2}}. \quad (2)$$

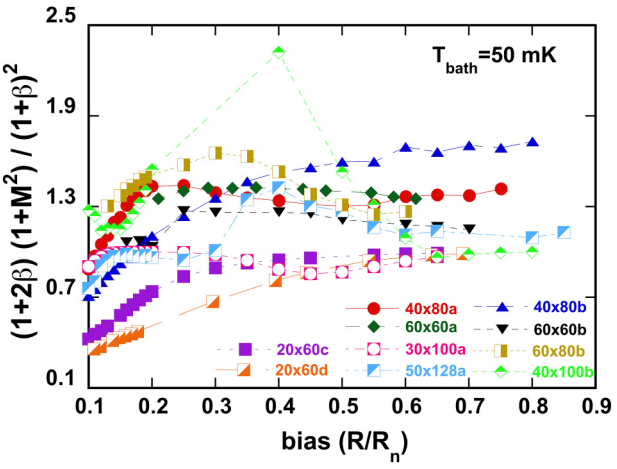

FIG. 9. Ratio $(1 + 2\beta)/(1 + M^2)/(1 + \beta)^2$ as a function of bias. This ratio should equal unity in the case of two-fluid dominated noise.

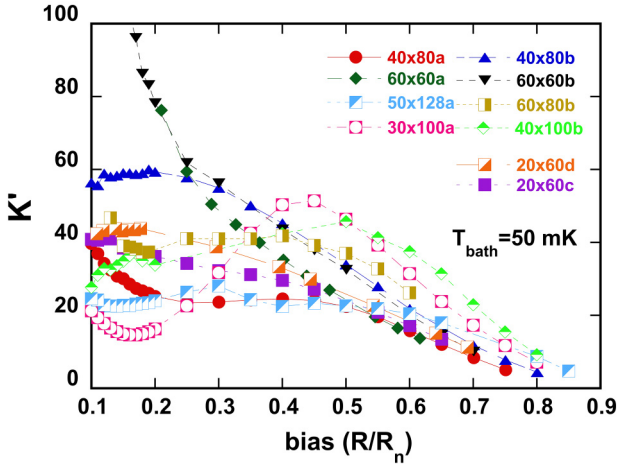

FIG. 10. Figure of merit K', as defined in the text [Eq. (2)], for all the devices with an absorber.

This figure of merit takes into account both the Johnson-like excess noise and the second order non-linearities.[22,46] Therefore, in Ref. 1, higher K' should correspond to better energy resolution. The graph confirms that TESs with larger w and outer tangent stems tend to yield better K' values, provided they are not excessively long. The best performance is seen in the 60×60b and 40×80b devices at low biases. In contrast, stems located on the area of the bilayer determined by the $w \times L$ rectangle and higher aspect ratios progressively reduce K'. These results reflect the balance between the opposite tendencies of α/β and M with respect to the stem position and aspect ratio: since most devices display quite low M values, α/β dominates the behavior of K'.

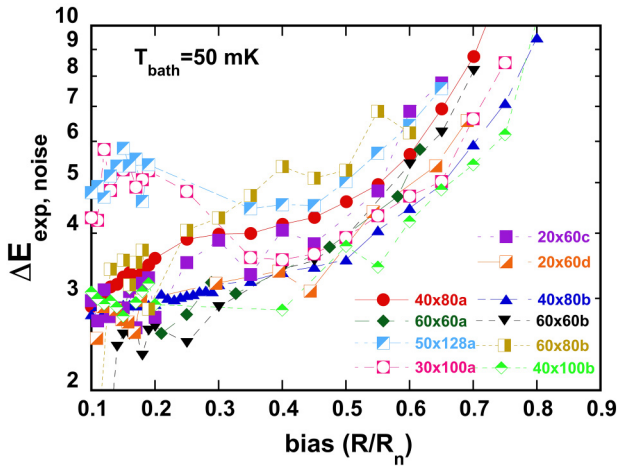

FIG. 11. Experimental spectral resolution, $\Delta E_{exp,noise}$ extracted from the noise spectra using Eq. (1), for all the devices with absorber.

Finally, Fig. 11 displays the spectral resolution derived from experimental noise, $\Delta E_{exp,noise}$. Comparison of both Figs. 10 and 11 shows that TESs with better K' generally exhibit lower $\Delta E_{exp,noise}$, as expected. A notable exception is represented by TESs 40×100b and 60×80b: the former has somewhat lower K' but a significantly higher $\Delta E_{exp,noise}$.

CONCLUSIONS

We have conducted a detailed analysis of the influence of absorber stem position and TES geometry on the key performance parameters and Johnson-like excess noise of high-quality Mo/Au TESs with gold absorbers.

The logarithmic sensitivities α and β are comparable to values reported by other research groups, and the Johnson-like excess noise M is generally low. Absorber stems located within the TES rectangular area are detrimental to α and β since they cause constrictions in the superconducting bilayer that distort current flow across the TES. This effect, however, diminishes as the TES width increases—for instance, the 60×60 TES with a central stem outperforms narrower TESs ($w = 20$–$30\,\mu$m) with outer or partially outer stems.

Among TESs with tangent outer stems, those with higher aspect ratios exhibit increased α and β values but also higher M. Since M tends to decrease with decreasing L and increasing w, TESs with aspect ratios greater than 2 show a lower figure of merit K' compared to more square-shaped devices, independent of the stem position. This is especially evident at low bias. Interestingly, TESs with the high aspect ratio and central stems display non-monotonous α and β behavior that results in improved K' at higher bias.

In conclusion, the best-performing TESs combine moderate aspect ratios, wider geometries, and outer absorber stems. Promising optimization strategies include (1) refinement of TES geometries with $w = 40$–$60\,\mu$m and $L = 40$–$80\,\mu$m, using outer tangent stems or (2) deeper investigation into the distinct excess noise behavior observed in narrow, high-AR TESs (e.g., 20×60).

Preliminary analyses using various noise models do not conclusively identify the dominant origin of the Johnson-like excess noise, particularly in TESs with internal stems. Internal thermal fluctuation noise and higher-order nonlinearities may govern M at low bias in devices with outer tangent stems, while at high biases, excess noise may be more consistent with the two-fluid model predictions.

SUPPLEMENTARY MATERIAL

See the supplementary material for optical microscope images of TESs, graphs of Z(ω) with fits, error bars on parameters extracted from Z(ω) fits, and a representative graph of noise and its contributions.

ACKNOWLEDGEMENTS

The Spanish Ministerio de Ciencia, Innovación y Universidades (MICIU) supports and funds this work, under Grant PID2021-122955OB-C42 (also funded by FEDER, UE), and Grants for Severo Ochoa Centers of Excellence CEX2023-001263-S and CEX2023-001286-S. We also acknowledge the Catalan Government

through Grant 2021-SGR-00445 and the Aragón Regional Government through project QMAD (E09 23R).

AUTHOR DECLARATIONS

Conflict of Interest

The authors have no conflicts to disclose.

Author Contributions

Lourdes Fàbrega: Conceptualization (lead); Formal analysis (lead); Methodology (lead); Writing – original draft (lead). **Agustín Camón:** Data curation (equal); Investigation (equal); Resources (equal). **Carlos Pobes:** Data curation (equal); Investigation (equal); Resources (equal). **Pavel Strichovanec:** Investigation (supporting); Resources (equal). **J. Bolea:** Data curation (supporting); Software (supporting).

DATA AVAILABILITY

The data that support the findings of this study are available from the corresponding author upon reasonable request.

REFERENCES

[1]K. D. Irwin and G. C. Hilton, "Transition-edge sensors," in *Cryogenic Particle Detection*, edited by C. Enss (Springer, Berlin, 2005), Vol. 99.
[2]P. Peille *et al.*, Exp. Astron. **59**, 18 (2025).
[3]J. G. Staguhn *et al.*, Proc. SPIE **13102**, 139–144 (2024).
[4]B. J. Rauscher *et al.*, J. Astron. Telescopes Instrum. Syst. **2**(4), 041212 (2016).
[5]B. Westbrook *et al.*, J. Low Temp. Phys. **216**, 264 (2024).
[6]L. Manenti *et al.*, Phys. Rev. Appl. **22**, 024051 (2024).
[7]R. K. Romani *et al.*, Appl. Phys. Lett. **125**, 232601 (2024).
[8]Y. H. Kim, S. J. Lee, and B. Yang, Supercond. Sci. Technol. **35**, 063001 (2022).
[9]G. Angloher *et al.*, J. Low Temp. Phys. **200**, 428 (2020).
[10]D. Fukuda and T. Kikuchi, Prog. Opt. **68**, 135 (2024).
[11]T. Gerrits, A. Lita, B. Calkins, and S. W. Nam, in *Superconducting Devices in Quantum Optics*, edited by R. Hadfield and G. Johansson (Springer, Cham, 2016), pp. 31–60.
[12]C. Pepe *et al.*, Phys. Rev. Appl. **22**, L041007 (2024).
[13]O. Quaranta *et al.*, IEEE Trans. Appl. Supercond. **35**, 2100605 (2025).
[14]D. A. Bennett *et al.*, Rev. Sci. Intrum. **83**, 093113 (2012).
[15]J. N. Ullom and D. A. Bennett, Supercond. Sci. Technol. **28**, 084003 (2015).
[16]L. Gottardi and K. Nagayoshi, Appl. Sci. **11**, 3793 (2021).
[17]M. de Lucia *et al.*, Instruments **8**, 47 (2024).
[18]J. N. Ullom *et al.*, Appl. Phys. Lett. **84**, 4206 (2004).
[19]N. Jethava *et al.*, AIP Conf. Proc. **1185**, 31 (2009).
[20]S. J. Smith *et al.*, J. Appl. Phys. **114**, 074513 (2013).
[21]S. Zhang *et al.*, J. Appl. Phys. **121**, 074503 (2017).
[22]K. M. Morgan *et al.*, Appl. Phys. Lett. **110**, 212602 (2017).
[23]Y. Zhou *et al.*, J. Low Temp. Phys. **193**, 321 (2018).
[24]N. A. Wakeham *et al.*, J. Low Temp. Phys. **193**, 231 (2018).
[25]A. R. Miniussi *et al.*, J. Low Temp. Phys. **193**, 337 (2018).
[26]N. A. Wakeham *et al.*, J. Appl. Phys. **125**, 164503 (2019).
[27]E. Taralli *et al.*, AIP Adv. **9**, 045324 (2019).
[28]Y. Zhou, J. Phys.: Conf. Ser. **1590**, 012032 (2020).
[29]A. Kozorezov *et al.*, J. Low Temp. Phys. **167**, 108 (2012).
[30]L. Gottardi *et al.*, Phys. Rev. Lett. **126**, 217001 (2021).
[31]A. Wessels *et al.*, Appl. Phys. Lett. **118**, 202601 (2021).
[32]M. Galeazzi, IEEE Trans. Appl. Supercond. **21**, 267 (2011).
[33]M. de Wit *et al.*, J. Appl. Phys. **128**, 224501 (2020).
[34]M. de Wit, Phys. Rev. Appl. **16**, 04459 (2021).
[35]E. Taralli *et al.*, J. Low Temp. Phys. **209**, 256 (2022).
[36]N. A. Wakeham *et al.*, IEEE Trans. Appl. Supercond. **33**, 2100506 (2023).
[37]M. Kounalakis, L. Gottardi, M. de Wit, and Y. M. Blanter, Phys. Rev. Appl. **20**, 024017 (2023).
[38]M. de Wit *et al.*, IEEE Trans. Appl. Supercond. **35**, 2100505 (2025).
[39]F. T. Jaeckel *et al.*, IEEE Trans. Appl. Supercond. **33**, 2100407 (2023).
[40]L. Fàbrega *et al.*, J. Low Temp. Phys. **209**, 287–292 (2022).
[41]A. Camón *et al.*, J. Low Temp. Phys. **222**, 27 (2026).
[42]M. Mas *et al.*, "Electrothermal modeling of Mo/Au transition-edge sensor" (2021), available at https://jphd.icmab.es/images/2021/posters/Poster_JPhD2021_Mas_Manel.pdf.
[43]D. C. Goldfinger *et al.*, J. Low Temp. Phys. **193**, 984–990 (2018).
[44]L. Fàbrega *et al.*, J. Appl. Phys. **136**, 154503 (2024).
[45]L. Fàbrega *et al.*, Supercond. Sci. Technol. **32**, 015006 (2019).
[46]S. Zhang *et al.*, J. Appl. Phys. **121**, 074503 (2017).